CHEMISTRY

The carrier transition from Li atoms to Li vacancies in solid-state lithium alloy anodes

Yang Lu[1], Chen-Zi Zhao[1,2], Rui Zhang[3], Hong Yuan[3], Li-Peng Hou[1], Zhong-Heng Fu[1], Xiang Chen[1], Jia-Qi Huang[3], Qiang Zhang[1]*

The stable cycling of energy-dense solid-state batteries is highly relied on the kinetically stable solid-state Li alloying reactions. The Li metal precipitation at solid-solid interfaces is the primary cause of interface fluctuations and battery failures, whose formation requires a clear mechanism interpretation, especially on the key kinetic short board. Here, we introduce the lithium alloy anode as a model system to quantify the Li kinetic evolution and transition from the alloying reaction to the metal deposition in solid-state batteries, identifying that there is a carrier transition from Li atoms to Li vacancies during lithiation processes. The rate-determining step is charge transfer or Li atom diffusion at different lithiation stages.

INTRODUCTION

Research into Li kinetics has spanned several decades since the invention of lithium batteries (*1*). Li kinetics in liquid electrolytes has been thoroughly investigated according to the laws of physical chemistry (*2*). Recently, with the booming of solid-state batteries with enhanced energy density and safety, Li kinetics is involved in the brand-new areas with solid-state ionics and electrochemistry (*3*, *4*). The solid-state lithium batteries still suffer from the uneven Li electrodeposits and dendrite-induced failure even with solid-state electrolytes having high mechanical strength. To overcome the dilemma, a basic understanding toward solid-state Li kinetics is essential to distinguish the rate-determining step in battery cycling. However, the research into solid-state Li kinetics confronts challenges. Conventional knowledge of Li kinetics in liquid-electrolyte systems exhibits discrepancies comparing with that in all-solid-state systems. The conventional Li kinetics for Li plating in liquid electrolytes includes the liquid diffusion, adsorption, solvation sheath breakup, ion transport in solid electrolyte interphase, charge transfer, and the subsequent atom diffusion on anodes (*5*). The possible rate-determining steps in liquid systems are the ion transport or desolvation processes. In solid-state systems however, there is a space charge layer comparable to the electric double layer in solvation systems (*6*). The special solid-solid contact and solid-state conduction will also influence the ionic flux, the mass transport, and interfacial reactions (*7*). Therefore, the electrochemical Li kinetic theories based on liquid systems cannot be completely inherited by solid-state systems. Because of the absence of liquid wetting, the mass transport relies on the solid-state diffusion, which is determined by special carriers (e.g., ions, atoms, or vacancies). Therefore, identifying the carriers for the Li mobility and the rate-determining step is essential to understand solid-state Li kinetics.

Mass transport and interfacial charge transfer are key processes in solid-state batteries (*8*). The intrinsic rapid charge transfer at ideal Li metal/electrolyte interfaces is proven by a high exchange current density of >300 mA cm^{-2} (*9*). Hence, the lithium diffusion determines the morphological stabilities (*10*). Nevertheless, the carriers of the Li mobility process and pivotal rate-determining step during the Li plating processes have not been determined due to the absence of a quantitative research. Among various lithium anodes, Li alloys can minimize the influence of the interfacial chemical reaction and also display different diffusion characteristics with different Li contents (*11*, *12*). Consequently, Li alloy anodes work as ideal model systems to investigate Li kinetic features with different lithiation stages. In addition, the Li alloy anode is also a strong candidate for next-generation energy-dense anodes. A quantitative investigation of Li kinetics in solid-state batteries will greatly promote their practical applications.

Here, we treat Li-In alloy as a model system for screening the rate-determining step and carrier species in Li kinetics. The kinetic transition from alloying to metal deposition is found, and their evolution processes are in situ monitored by galvanostatic electrochemical impedance spectra (GEIS) analyzed by distribution of relaxation time (DRT). The Li atomic diffusion and charge transfer are quantified and compared during the whole lithiation process, indicating the rate-determining step of lithiation processes. The rapid Li atomic diffusion (>10^{-11} cm^2 s^{-1}) and a rapid charge transfer avoiding Li metal nucleation guarantee the stable alloying process, while the decayed charge transfer will trigger the transition from alloying to metal deposition. The kinetic transition indicates the alternation of carriers in bulk diffusion from Li atoms to Li vacancies, which determines the electrochemical and morphological stabilities.

RESULTS

The lithiation process

The lithiation behaviors of Li-In alloy in continuous lithium plating are shown in Fig. 1, which are conducted with $Li_7P_3S_{11}$ sulfide solid-state electrolytes (SSEs) with a high ionic conductivity. The whole lithium plating process exhibits three obvious plateaus in Li-In alloy, delivering the voltages of 0.59, 0.32, and −0.10 V under a current density of 1.0 mA cm^{-2} (Fig. 1A). The smooth lithiation profiles of Li_xIn ($x < 1.25$) demonstrate a stable Li plating process in a Li-In alloy. A drastic fluctuation at the third discharge plateaus can be observed, indicating a failure of the Li-In alloy. The Li content at $x = 1.25$ separates the profiles of stable and unstable regions. Therefore, this Li content is defined as the critical Li contents of a Li-In alloy. The corresponding phase compositions are displayed in

[1]Beijing Key Laboratory of Green Chemical Reaction Engineering and Technology, Department of Chemical Engineering, Tsinghua University, Beijing 100084, China. [2]State Key Laboratory of Automotive Safety and Energy, School of Vehicle and Mobility, Tsinghua University, Beijing 100084, China. [3]Advanced Research Institute of Multidisciplinary Science, Beijing Institute of Technology, Beijing 100081, China. *Corresponding author. Email: zhang-qiang@mails.tsinghua.edu.cn

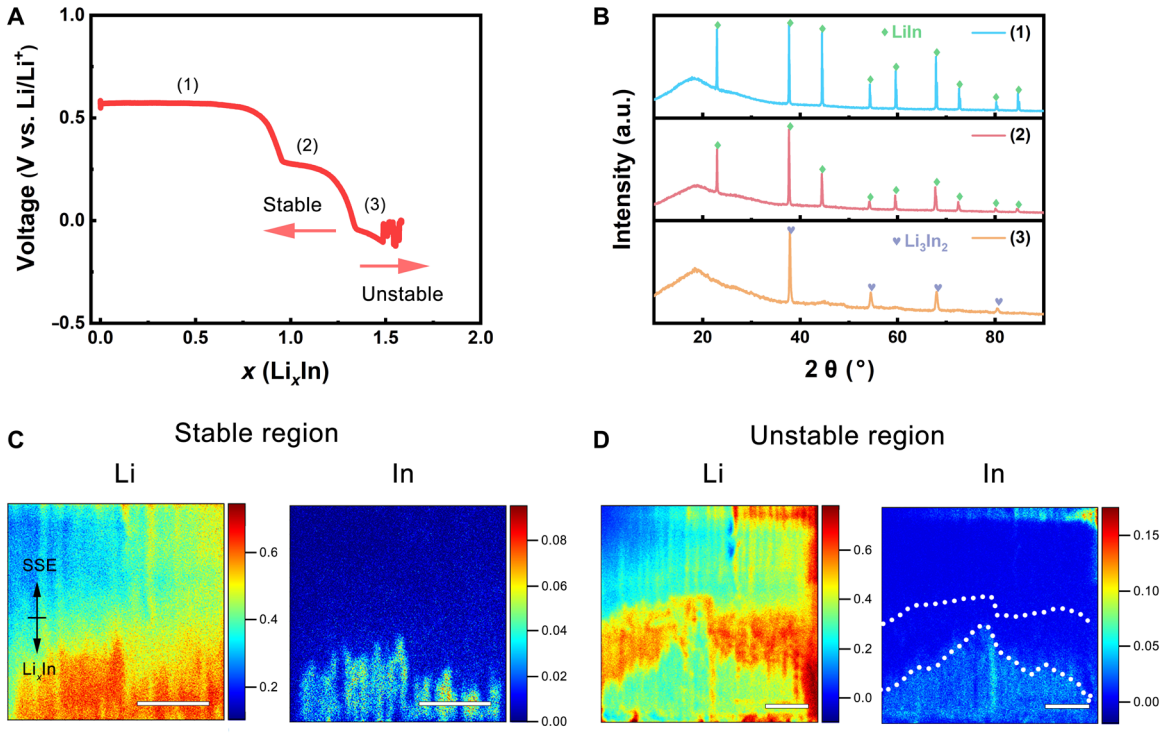

Fig. 1. Lithiation behaviors of Li-In alloy. (**A**) Voltage profiles of Li-In alloy during the lithiation process. (**B**) XRD patterns of Li-In alloy at different lithiation stages, which are in accordance with the profiles labeled with (1) to (3) in (A), respectively. a.u., arbitrary units. (**C** and **D**) Cross-sectional elemental mapping of Li and In by time-of-flight secondary ion mass spectroscopy (TOF-SIMS). (C) Elemental distributions at a stable lithiation stage ($x = 1.0$ in Li_xIn) and (**D**) those at failure stages ($x = 1.5$ in Li_xIn). Scale bars, 10 μm.

Fig. 1B. The first and second discharge plateaus show a major phase of LiIn with some discrepancies on peak intensities. Subsequently, the phase compositions convert into Li_3In_2 at the third discharge plateau. These results prove the occurrence of phase transitions with increasing lithium contents. In addition, the interfacial properties between SSEs and Li-In alloy are unraveled by x-ray photoelectron spectroscopy. We compare the In three-dimensional results of the initial Li-In phase (first discharge plateau) and final stages (third discharge plateau) in fig. S1. Their interfacial properties demonstrate the existence of Li-In alloy (442.8 and 449.8 eV) and In_2S_3 (444.2 and 451.5 eV) (*13*).

Meanwhile, the interfacial lithium distribution is highly depended on the lithium contents. To detect the interfacial Li distributions, the time-of-flight secondary ion mass spectroscopy (TOF-SIMS) is conducted to probe Li and In distribution on the cross section of alloy/SSE interfaces at different lithiation stages. The focused ion beam (FIB) technique is used to cut a cross section of Li-In/SSE interface for TOF-SIMS imaging (fig. S2). Figure 1C exhibits the TOF-SIMS mapping of Li, which delivers a homogeneous interfacial Li distribution with low lithium contents ($x = 1$ in Li_xIn). The color intensity from red to blue represents the relative element concentration. Comparatively, local Li accumulation can be identified at the electrode-electrolyte interfaces in the lithiation stage over critical Li contents ($x = 1.5$ in Li_xIn; Fig. 1D). The signals of indium clearly distinguish the interface regions. Li signals at the interfaces demonstrate the termination of Li alloying process with the emerging of Li metal. It is proved that the critical Li content plating induces the Li precipitation failure.

The LiIn alloy electrodes under various lithiation stages exhibit different electrochemical cycling behaviors. Figure S3 indicates that the polarization of a Li_2In electrode (400 mV) is 10 times that of a LiIn electrode (40 mV). Moreover, LiIn electrodes can achieve a high Coulombic efficiency of 99% (fig. S4A), however, the Coulombic efficiency of Li_2In anodes is reduced to 71% (fig. S4B). Hence, the Li contents in alloy anodes can greatly regulate the interfacial electrochemical processes.

Charge transfer evolution

The drastic changes of electrochemical features are derived from Li kinetic evolution, which is unraveled by applying the in situ GEIS methods with DRT analysis (*14*–*16*). Typical EIS is composed of an incomplete semicircle corresponding to the grain boundary of SSEs and an integrated semicircle corresponding to Li-In electrodes and interfaces. The impedance evolutions are divided into four stages, which are displayed in Fig. 2. The initial stage is displayed in Fig. 2A. The semicircles exhibit continuous shrinking at the initial stages of the whole first discharge plateau (Li_xIn, $0 < x < 1$), delivering an impedance decrease from 30 to 8 ohm. Then, the semicircles gradually expand at the second discharge plateau, delivering an increasing value from 15 to 50 ohm (Fig. 2B). The Li kinetics changes drastically with Li content of $x > 1.2$ in Li_xIn. Figure 2C exhibits that the impedances rapidly increase to >600 ohm between the transition from the second plateau to the third plateau. The total impedance reaches the highest value at the critical Li contents point between the second plateau and the third plateau. Last, the impedance shape is alternated to a small semicircle with an impedance of about

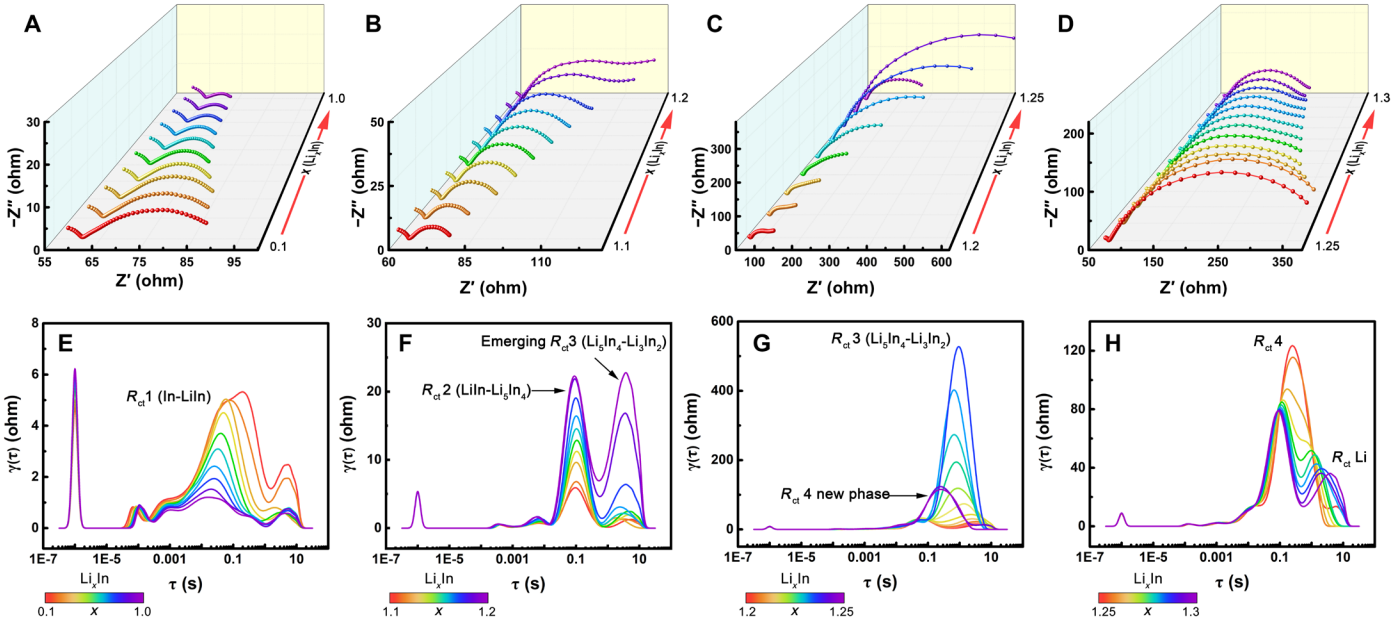

Fig. 2. Li kinetic evolutions in Li-In during continuous lithiation processes. GEIS on Li_xIn of (**A**) $0 < x < 1$, (**B**) $1.1 < x < 1.2$, (**C**) $1.2 < x < 1.25$, and (**D**) $1.25 < x < 1.3$, respectively. (**E** to **H**) Corresponding DRT transformation of GEIS results in (A) to (D) to unravel the charge transfer evolution.

250 ohm (Fig. 2D). The subsequent impedance with irregular data points represents the alloy failure (fig. S5).

To distinguish the specific electrochemical processes avoiding the manual simulation, here, the DRT technology is used, which is a model-free analysis toward the impedance evolutions. It is a mathematical transformation to display the frequency domain–based Nyquist plots into time domain–based DRT spectra (*17*, *18*)

$$Z(\omega) = R_\infty + \int_0^\infty \frac{\gamma(\tau)}{1 + j\omega\tau} d\tau \quad (1)$$

The whole EIS spectra will be converted as a relaxation-based function $\gamma(\tau)$. The peaks at special relaxation time represent the related specialized electrochemical process, and the peak areas represent the impedance value. The schematic mechanism of DRT is displayed in fig. S6. Hence, different specialized relaxation times can be automatically distributed.

The DRT successfully distributes the electrochemical phase transitions of Li-In alloy and their respective evolutions on impedance with increasing Li contents. The relaxation time identifications of different electrochemical processes are first conducted, and the detailed methods are introduced in Supplementary Materials (*14*). The τ at 10^{-6} s represents the grain boundary response of SSEs (fig. S7). The influence of the counter electrode can be excluded due to the weak response by DRT (fig. S8). It is ensured that three major peaks located at 10^{-5} to 10^{-4}, 10^{-2} to 10^{-1}, and 10 s exhibit obvious electrochemical processes for Li-In (Fig. 2E). As displayed in fig. S9, the peaks at 10^{-5} to 10^{-4} s represent an irreversible evolution, which can be attributed to the solid electrolyte interphase (SEI) formation. The stabilized value can be attributed to the ionic transport at the interfacial SEI which is denoted as R_{int}. The relaxation processes located at 10^{-2} to 10 s are all highly reversible (fig. S10), which represents the charge transfer processes (R_{ct}). The impedance spectra in Fig. 2 (A to D) are interpreted as DRT functions in Fig. 2 (E to H), respectively. The R_{ct} is continuously decreasing during the lithiation process in Li_xIn ($0 < x < 1$), which is labeled as $R_{ct}1$ (Fig. 2E). There are two charge transfer processes at the second plateau transition of Fig. 2F. Initially, the new charge transfer impedance ($R_{ct}2$) located at τ of 0.1 s gradually increases, which is corresponding to the lithiation process in LiIn to Li_5In_4 (Li_xIn, $1.1 < x < 1.16$). The third charge transfer processes ($R_{ct}3$) located at τ of 5 s rapidly emerge and increase at the end of second plateau lithiation, which indicates the beginning of the transition from Li_5In_4 to Li_3In_2 (Li_xIn, $1.17 < x < 1.2$). The $R_{ct}3$ of complete lithiation transition from Li_5In_4 to Li_3In_2 increases sharply. The electrochemical processes are reflected by the continuous peak evolutions at τ of 1 to 5 s displayed in Fig. 2G.

Afterward, the electrochemical processes completely change after reaching critical Li contents of $x = 1.25$. A new DRT peak with τ of 0.2 s (purple curve in Fig. 2G) is corresponding to a new $R_{ct}4$, which should be attributed to the R_{ct} of pure Li_3In_2. There are electrochemical evolutions at the third lithiation plateau. The DRT plots in Fig. 2H exhibit the peak-split processes under continuous plating. The split peaks at $\tau = 10$ s indicate the emerging of Li (R_{ct} Li), and another peak indicates the alloying process. At this stage, there are the alloying and Li deposition processes according to the DRT analysis. The phase transitions during the lithiation contribute to the increasing on the R_{ct}, which results in the evolution of overpotential.

The overview of the overpotential evolution is also displayed by the galvanostatic intermittent titration technique (GITT) profiles (*19*). The polarization exhibits three stages (fig. S11). There is a stable polarization of 17 mV in Li_xIn ($0 < x < 1$). Then, a gradual polarization increases at the region of $1 < x < 1.25$ of Li_xIn, which can subsequently reach a maximum polarization voltage of 300 mV. Last, an 80- to 100-mV polarization remains until the failure. The critical Li content point is exactly corresponding to the maximum polarization.

The unstable fluctuated profiles at third lithiation stage of in Li-In alloy are ascribed to the inhomogeneous Li precipitation–induced dendrite formation. The cycled Li-In alloy is measured by TOF-SIMS to provide the surficial properties (fig. S12), where the typical

stable phase of LiIn and unstable phase of $Li_{1.5}In$ are compared. The synchronous intensity of Li and In signal on LiIn phase demonstrates the stable alloying property. The signal P proves the homogeneous SEI. In contrast, severe Li accumulation is detected with the relative weak In intensity, demonstrating the existence of the inhomogeneous precipitation of Li metal.

Subsequently, the fluctuation of discharge profile is monitored by the GEIS. As displayed in fig. S13A, the smooth profile represents the stable kinetics and the fluctuation demonstrates the battery failure. Six measurement points marked in fig. S13A show the evolution processes. Because of the dendrite penetration, the impedance of SSEs will be continuously reduced (fig. S13B). The points at the frequency of >16 kHz represent bulk resistance of SSEs (fig. S13C). The failure impedances exhibit the reduced SSE impedance at high frequency and abnormal points for Li kinetics (fig. S13D). The mess points on the impedance demonstrate the soft short circuit. The reduced high-frequency impedance of SSEs proves the Li dendrite formation (fig. S13E). During the stable process, the bulk SSE impedance remains stable. The bulk SSE impedance drops after the failure, proving the continuous Li dendrite penetration.

Diffusion evolutions

As shown in Fig. 3A, the major Li kinetics at solid-state interfaces contains three steps, including (1) Li^+ transport in SSE, (2) interfacial charge transfer process, and (3) Li atom diffusion in bulk Li alloys or Li metal. The lithium ion diffusion in sulfide SSEs ($>10^{-9}$ cm^2 s^{-1}) is faster than the mass transport of Li atoms in bulk alloy anode (*10*, *20*). Therefore, the chemical diffusion and charge transfer of lithium atoms are inferred as rate-determining steps.

The continuous kinetic evolution is controlled by the increasing Li contents, according to the R_{ct} evolution. The Li kinetics is also deduced from Bulter-Volmer equation. The relationship among charge transfer impedance, interfacial Li atom (Li^0) concentration, and the reaction rate constant k_0 is described in Eqs. 2 and 3 (*21*)

$$R_{ct} = \frac{RT}{Fi_0} \quad (2)$$

$$i_0 = nFk_0[Li^+]^{\alpha_a}[Li^0]^{\alpha_c} \quad (3)$$

Here, the R_{ct} is in inverse proportion to exchange current density i_0. The α_a and α_c represent the anodic and cathodic transfer coefficient, respectively. As displayed in Eqs. 2 and 3, the R_{ct} is directly related with k_0 and Li^0 concentration. Hence, R_{ct} can reflect the interfacial concentration evolution in same alloy phases. It has been proposed that the interfacial lithium atom concentration in Li alloy influences the charge transfer impedance, and the relaxation of R_{ct} was observed (*10*).

Equation (3) describes the fact that the interfacial kinetics is depended on the Li atom concentration. Hence, the GITT coupled with GEIS is conducted to unravel the Li atom diffusion evolution. The specific relaxation stages are marked as *a* to *h* in fig. S11. The relaxation of EIS at different stages can directly reflect the interfacial Li atom diffusion in alloy (fig. S14).

The rapid relaxation is detected at the initial lithiation stages ($0 < x < 1$ of Li_xIn, position *a*). The overlapped impedance proves the rapid diffusion resulting in the balanced interfacial Li concentration (fig. S14A). Then, obvious relaxation of R_{ct} gradually emerges, corresponding to a reduction of interfacial Li concentration at the beginning of the second plateau (position *b*). The lithiation stages from positions *b* to *d* (fig. S14, B to D) exhibit similar processes, but the relaxation processes gradually slow down. The high impedances prove the sluggish kinetics (positions *e* and *f*), and the prolonged relaxation demonstrates the diffusion fading, which are demonstrated in fig. S14 (E and F). Last, the relaxation processes almost disappear (positions *g* and *h*; fig. S14, G and H). The DRT can interpret the diffusion degradation of specific R_{ct} in detail (fig. S15). These relaxation processes directly show the diffusion degradation from a rapid diffusion, subsequent sluggish diffusion, to the almost immobility in continuous lithiation processes.

According to the GITT profiles, it is calculated that the stable region is corresponding to a stable Li atom diffusion coefficient D_{Li^0} of 10^{-10} cm^2 s^{-1} and can reach the highest D_{Li^0} more than 10^{-9} cm^2 s^{-1} at the initial plateau. Subsequently, D_{Li^0} will gradually decay to 10^{-12} cm^2 s^{-1} until the critical Li contents between the second and third plateau. Considering the self-diffusion coefficient of Li is measured at 10^{-11} cm^2 s^{-1} (*10*, *22*, *23*), the Li kinetics includes the competition between the alloying and the deposition. The vanishing of chemical diffusion can promote the kinetic transitions from the alloy lithiation to the lithium deposition, which is also a rational interpretation of the sudden change of R_{ct} in Fig. 2G.

The kinetic transition also indicates the transition of the dominated carriers from Li atoms to Li vacancies. Two fundamental types of diffusion in solid are interstitial diffusion and the vacancy diffusion with different domination carriers. The colored areas in Fig. 3B exhibit the different Li kinetics stages. First, the Li atoms are gradually diffusing into the indium matrix in alloys. In general, the conductive abilities are expected to be enhanced with increased the carrier concentrations (*24*). However, the drastic impedance climb neighboring

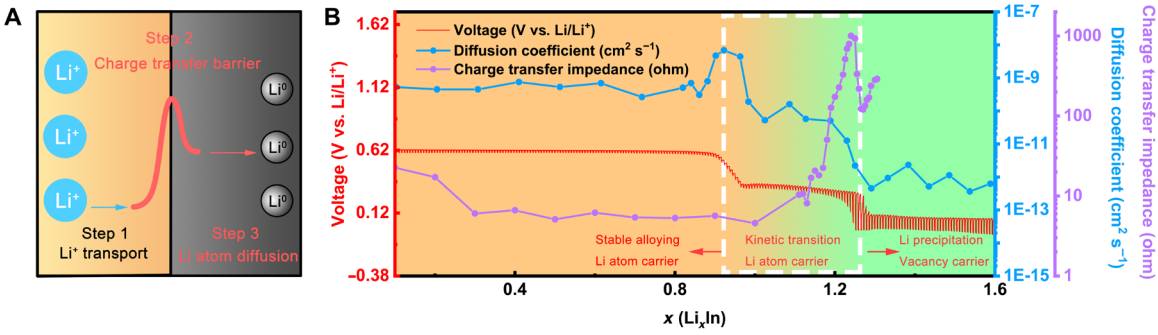

Fig. 3. The evolution of diffusion abilities. (**A**) Schematic of the key interfacial Li kinetic processes. (**B**) Evolution of diffusion coefficient (blue line) and total R_{ct} (purple line) accompanied with GITT profiles. The filling colors exhibit the carrier transition from Li atoms to Li vacancies.

Li_xIn ($x = 1.25$) indicates that Li atoms mobility is abruptly retarded, after which the carriers are altered from Li atoms to Li vacancies. The critical Li contents with the highest impedance indicates the Li kinetic transition from alloying to metal deposition. These measurements also provide quantified parameters for phase field simulations of the whole lithiation processes.

DISCUSSION

Mechanisms

The phase field method was introduced to simulate the Li kinetics in alloy anodes, unraveling the dynamic phase transition including both mass transport and diffusion kinetics, especially the lithium precipitation in continuous lithiation stages (*25*). The phase field models consider the electrostatic field and concentration diffusion field simultaneously to provide a key parameter as phase field parameter x to describe the specific phase with different Li contents (*26*). Here, the x of <0 represents the ionic stage of Li^+. The $x > 0$ matches the stoichiometric ratio x of lithium in the Li_xIn. For instance, the $0 < x < 1$ represents the In/LiIn alloy phase, and the specific $1 < x < 1.5$ presents the Li_xIn ($1 < x < 1.5$). The pure lithium metal is determined by $x > 1.5$. The dynamic processes of simulated Li distribution are displayed in Fig. 4, and the simulation details are displayed in the Supplementary Materials (fig. S16) (*15*). The model describes a homogeneous Li distribution at $x < 1$ in Li_xIn. The Li_xIn with $x > 1.25$ has represented the tendency on interfacial Li accumulation and the evolution of subsequent concentration and the final Li precipitation at a critical Li content of $x = 1.5$ in Li_xIn. The equilibrium potential of Li_3In_2 is 0.12 V versus Li/Li^+ (*27*). As measured in Fig. 3, the real overpotential (>300 mV) at critical Li contents ($x = 1.25$) has obvious covered the alloying potential of Li_3In_2, which will lead to the direct Li plating. The Li metal and Li_3In_2 will generate simultaneously after the critical Li contents. The simulated results are in accordance with the TOF-SIMS images that a Li precipitation will emerge at the interface between the alloy and the SSEs at the later lithiation period.

The Li kinetic transition is highly related with the charge transfer and Li^0 diffusion, which are determined by the intrinsic phase with specific Li contents. The active carriers on distinguishing the diffusion or deposition can also be identified. The first derivatives of Li^0 diffusion coefficient and impedance are displayed in Fig. 5A, exhibiting their change rate with increasing Li contents. The turn point of the evolution on Li^0 diffusion is located at $x = 1$ in Li_xIn, and the turn point of the evolution on charge transfer impedance is located at the critical Li contents ($x = 1.25$ in Li_xIn). Hence, the charge transfer and Li^0 diffusion dominate the Li kinetics in different lithiation stages, respectively. The charge transfer directly influences the kinetical barrier for alloying stages, and the Li diffusion capability determines the carriers.

Initially, the Li-In alloy exhibits a stable alloying process. Stable alloying process remains because the high Li^0 diffusion coefficient (10^{-10} cm^2 s^{-1}), which is much higher than that of Li metal (10^{-11} cm^2 s^{-1}). Low R_{ct}-induced low overpotential (50 to 80 mV) guarantees a stable potential higher than 0 V versus Li/Li^+. There is no kinetic transition at this stage. The Li kinetic transition can be judged by a high charge transfer–induced Li precipitation potential (< 0 V versus Li/Li^+) and Li^0 diffusion capability which is lower than that in Li metal (10^{-11} cm^2 s^{-1}). Both of them exhibit advantages against the boundary condition for Li deposition factor at present lithiation stage. When the Li alloy stays at stable lithiation stages, the μ_{Li} in the alloy is obviously lower than that of Li metal, which dominates the alloying tendency. In addition, the intrinsic low nucleation and reaction barriers at the initial lithiation stage of Li alloy contribute to low R_{ct} with low overpotential (*28*). The lithiation stage with low Li contents exhibits a stable interface (Fig. 5B), which is related to the orange zone in Fig. 3B.

The charge transfer is the rate-determining step for Li kinetic transition at critical Li contents. The evolution turn point for the charge transfer is located at the critical Li contents ($x = 1.25$ in Li_xIn). The high charge transfer impedance for alloying processes with high Li contents requires additional driven force, accompanying with a high reaction overpotential (*29*). The total Li chemical potential μ_{Li}

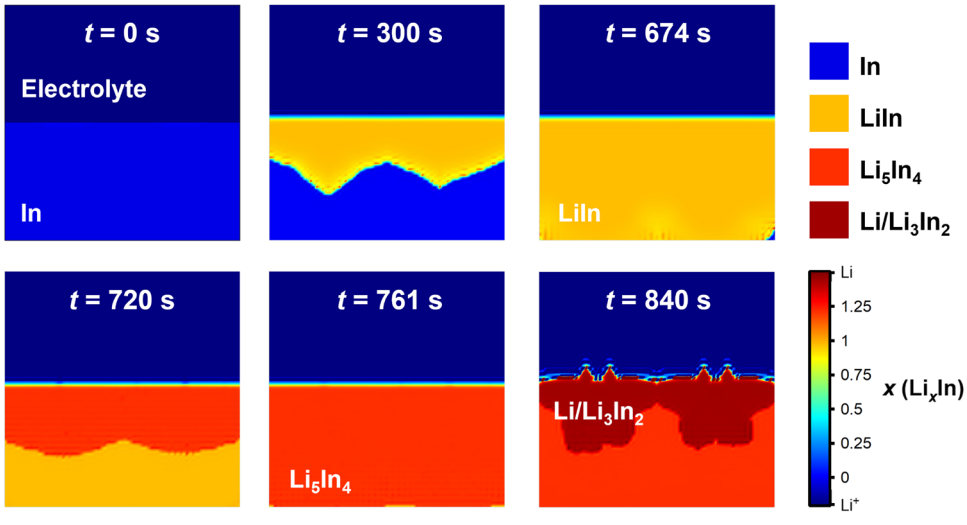

Fig. 4. Phase field simulation of Li concentration distribution during lithiation processes. Phase field–simulated evolution process of Li_xIn alloy with a constant lithiation current density of 5 mA cm^{-2}, displaying the lithium concentration distributions and the new phase emerges.

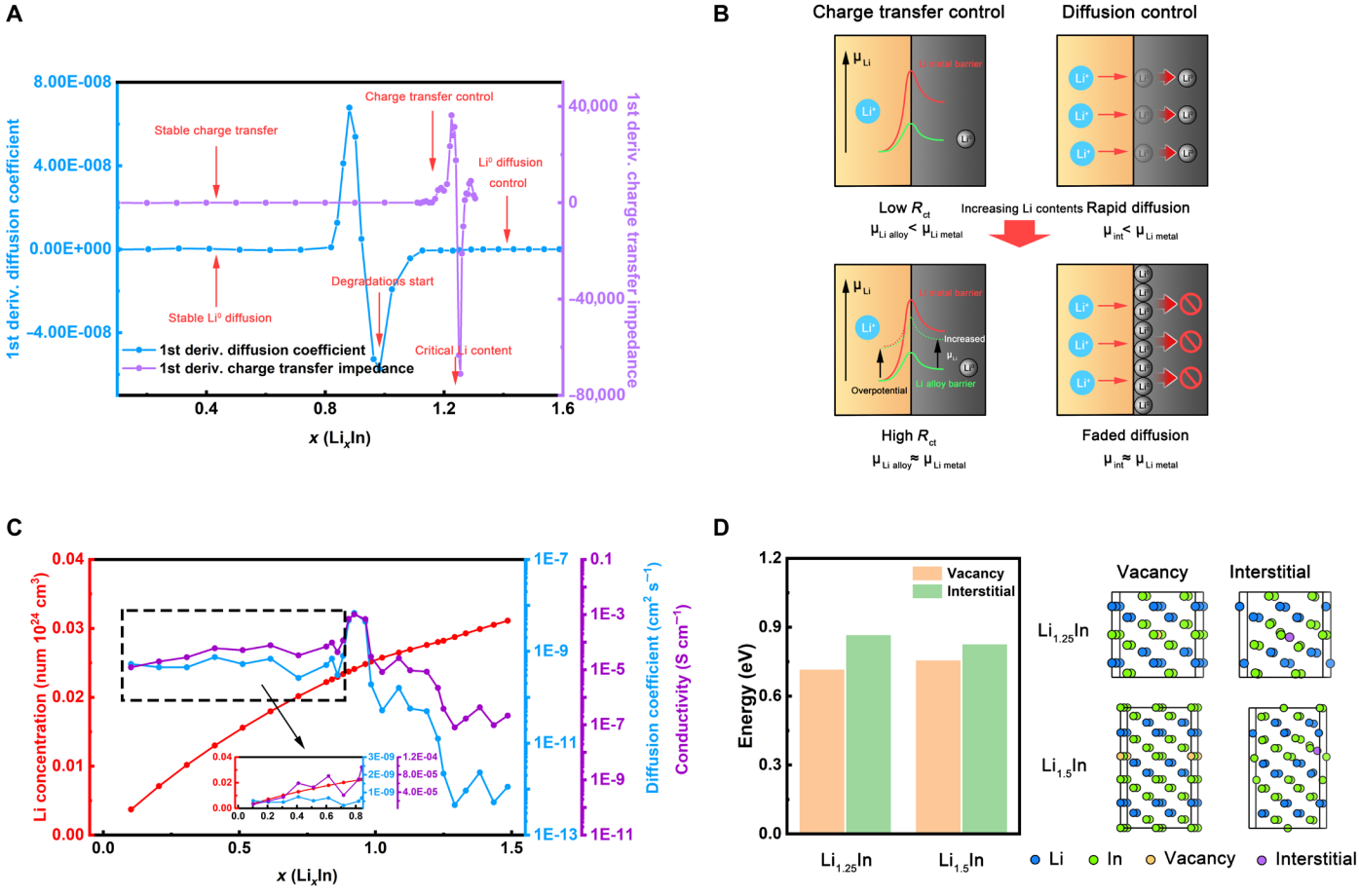

Fig. 5. Rate-determining steps and major carriers for Li kinetic transition. (**A**) First derivatives for the evolutions of the Li^0 diffusion coefficient and charge transfer impedance in Fig. 3B. (**B**) Schematic of Li kinetics in alloy anodes. Stable alloying during $x < 1$ in Li_xIn. The charge transfer dominates the Li kinetics during the alloying process ($1 < x < 1.25$ in Li_xIn). The Li atom diffusion is the rate-determining step for kinetic transition with exceed Li contents of the critical Li content ($x > 1.25$ in Li_xIn). (**C**) Evolution of Li concentration (red), diffusion coefficient (blue), and conductivity (purple) in Li-In alloy during continuous lithiation. (**D**) Vacancy and interstitial formation energy for Li-In alloy with high Li contents and atomic structures with vacancies or interstitial atoms of $Li_{1.25}In$ and $Li_{1.5}In$.

in Li alloy is continuously increasing during the rise of Li concentrations (*30*) and will reach the equivalent standard of that in Li metal. Considering the overpotential for Li metal nucleation, the high overpotential will add additional μ_{Li} of Li alloy and stimulates the instantaneous kinetic transition from alloying to metal deposition (Fig. 5B, left), which is related to the gradient color zone (white dotted box) in Fig. 3B.

Subsequently, Li kinetics in the next stage is dominated by the Li^0 diffusion. Unlike the real-time response of charge transfer, the Li^0 diffusion exhibits a cumulative effect. As displayed by first derivatives of Li^0 diffusion coefficient, the Li precipitation–induced failure exhibits a hysteresis comparing with the diffusion degradation. The charge transfer impedance becomes small after the critical Li contents point, and the overpotential recovers to a lower value (80 to 100 mV), which reduces the reaction barrier for Li precipitation. Hence, the preservation of interfacial Li metal is attributed to the Li^0 diffusion at this lithiation stage ($x > 1.25$ in Li_xIn). Here, Li^0 diffusion works as the rate-determining step at this lithiation stage. A high diffusion capability ($>10^{-11}$ cm^2 s^{-1}, intrinsic Li^0 diffusion capability of Li metal) can help to reduce the interfacial Li^0 concentration. Therefore, the interfacial Li chemical potential μ_{int} can remain stable with rapid diffusion, realizing the mass balance between Li^+ and Li^0. The low potential Li alloy (e.g., Li-Mg with potential of ~0 V versus Li/Li^+) can still remain stable alloying due to the satisfied Li^0 diffusion capability ($>10^{-11}$ cm^2 s^{-1}) (*10*, *31*). Virtually, the alloy phases with increased Li contents deliver a reduced internal diffusion pathway, relating to a reduced diffusion coefficient. Therefore, the weakened diffusion capability with nearly 0 V versus Li/Li^+ will lead to the increased interfacial Li concentration during lithiation, reflecting the enhanced μ_{int}. If the diffusion coefficient of Li alloy is reduced to a lower level than that in Li metal, the major advantages of Li^0 chemical diffusion will vanish in Li alloy anode. An interfacial mass mismatch of Li^+/Li^0 will occur, which prompts the Li precipitation and accumulation, consolidating the result of Li kinetic transition. The basic diffusion kinetics will be completely altered, and the transition of carrier dominates the changes. This lithiation stage is related to the green zone in Fig. 3B.

Here, the identification toward major carriers is relied on electrochemical and solid-state physics analysis, which is highly related with the dynamic driven force. The driven force determines the mobility of carriers. During the electrochemical process, distinguishing from the intrinsic thermal dynamic diffusion, the mass transport in

Li alloy for battery operation is mainly driven by the Li chemical potential gradient. Here, unraveling the major carriers in Li alloy/metal mainly means to identify the carriers toward Li chemical potential in the metal electrodes. The Li chemical potential can influence the interfacial electrochemistry (*10*). As displayed in fig. S14, obvious interfacial relaxation during lithiation can be detected, demonstrating the existence of Li chemical potential gradient on changing the interfacial Li chemical potential, which directly transports the interfacial Li atom concentration of Li alloy after lithiation (*10*). The carriers for Li kinetics will be Li atom which can move down the Li chemical potential gradient during the alloying process. In addition, according to Nernst-Einstein (Eq. 4), the conductivity is basically proportional to the carrier concentration (*32*). It is a major criterion to identify the major carrier (*33*). The Li atoms in alloy during the lithiation and delithiation are mostly reversible. Hence, the Li atoms in alloy are mobile species during the electrochemical processes, and their concentration can be measured. According to this equation, we calculated the conductivity σ(*T*) during different lithiation stages in the view of the whole alloy

$$\sigma(T) = \frac{N_{\mathrm{Li}} e^2}{V k_{\mathrm{B}} T} D(T) \tag{4}$$

N_{Li} is the number of Li species and V represents the unit volume for calculation. e is the electronic charge. k_{B} represents the Boltzmann constant. T is the application temperature. $D(T)$ represents the diffusion coefficient. The evolution tendency of the concentration, diffusion coefficient, and conductivity are displayed in Fig. 5C. The diffusion coefficient is derived from the GITT evaluation. As calculated, with the $x < 1.0$ in Li_xIn, the diffusion coefficient almost remains stable. The Li conductivity in Li alloy exhibits a linear increasing which is synchronized with the increasing of Li concentration (inset in Fig. 5C). Those can prove that Li atoms work as carriers that moves down the Li chemical potential gradient at $x < 1.0$ in Li_xIn stage).

Afterward, the Li concentration in Li-In alloy ($x > 1.0$ in Li_xIn) still increases, but the conductivity begins to drop, demonstrating the tendency on the transition of the carriers. The reduced diffusion coefficient means to the weakening of chemical potential gradient, reducing the capability of Li atoms to moving down the Li chemical potential. Until the potential is lower than 0 V versus Li/Li^+, the Li chemical potential gradient vanishes in bulk metal. The major driven force for mass transport will be altered from chemical potential gradient to the intrinsic thermal dynamic processes. The carriers for the mass transport are driven by physical thermal motions. Hence, vacancies or interstitial atoms are possible thermal dynamic carriers.

Practically, the transition of $x > 1.25$ in Li_xIn always happens at the potential of <0 V versus Li/Li^+. As displayed in Fig. 5D, we compare the vacancy formation energy and interstitial formation energy of high Li contents Li-In alloy by the density functional theory (DFT) calculation. As calculated, the $Li_{1.25}In$ and $Li_{1.5}In$ have the vacancy formation energies of 0.72 and 0.76 eV, respectively, and the related interstitial formation energies are 0.87 eV of $Li_{1.25}In$ and 0.83 eV of $Li_{1.5}In$. Their vacancy formation energies are lower than their interstitial formation energies, proving the tendency of vacancy dominated mass transport. Considering the Li metal with vacancies as carriers delivering vacancy formation energy of 0.54 eV (*34*), vacancies are ensured as carrier at the stage with low chemical potential gradient stage with high Li content alloys and the emerged Li metal.

These kinetic evolution characteristics can also be reflected in other alloy systems. The Al and Sn as typical alloying type substrates are also evaluated. Similarly, the lithiation of Al in all-solid-state batteries also exhibits a single Li alloying plateau and a subsequent unstable degradation until battery failure (fig. S17). The Li-Al similarly displays a stable lithiation process with stable impedance (fig. S18). Subsequently, an obvious impedance transition point appeared (Fig. 6A, green to purple). This point of specific Li contents ($x = 1$ for Li_xAl) can be attributed as the critical Li contents of Li-Al alloy. The bulk impedance is fallen subsequently after the critical Li contents, indicating the dendrite penetration.

The DRT analyses unravel the interfacial evolution and the emerging new phase. As displayed in Fig. 6B, the τ at 10^{-5} s represents the feature of Li-Al/SSE interfaces. The fading of this specific peak demonstrates the interfacial transition. A specific R_{ct} at τ of about 8 s represents the emerging of Li metal. A distinct Li accumulation in Li-Al is also identified by TOF-SIMS, which is similar to that in the final lithiation stage of Li-In (Fig. 6C). The final phase of Li-Al can be attributed to Li metal due to the similar characteristics of R_{ct} and their DRT peaks and the TOF-SIMS results. As shown in fig. S19, the Al only forms the LiAl in solid-state batteries at room temperature but not a high Li content phase such as Li_3Al_2, Li_9Al_4, etc. These high Li contents phases can only form at high temperature, and then the intrinsic low diffusion is an important limiting factor (*35*). It has been reported that the diffusion coefficient of Li atom is also decreased in Li-Al alloy with the increasing Li contents (*24*, *36*). The results for Sn substrates consolidate the understandings (fig. S20). A high capacity of 8 mAh can be realized by the alloying process, showing similar stable alloying stage and the failure stage (fig. S20A). Continuous impedance evolution can be detected (fig. S20, B and C). Especially, the impedance transition can be found (purple curve in fig. S20C). Subsequently, the failure impedance is displayed in fig. S20D. The DRT plots unravel the continuous the stable alloying and the transition process (fig. S20, E and F). Now, three kinds of alloying type metal have been measured (In, Al, and Sn) and exhibited similar transition process, proving the generality of the kinetic characters.

The metal substrates having nonalloying effects (Ti and Cu) are also measured to emphasize the importance of the Li chemical diffusion. As displayed, direct Li deposition is the only kinetic process (fig. S21). The deposition profile exhibits a short-term stable operation delivering a low capacity of 0.075 mAh (fig. S21A). The impedance of Li deposition remains similar before the failure (fig. S21B). However, the battery failure is proved by the impedance, and the impedance of bulk SSE will be continuously reduced by the Li dendrite penetration (fig. S21C). The Li deposition on Cu substrates exhibits the same process from the short stable deposition to the rapid failure (0.25 mAh; fig. S21D), including no kinetic transition (fig. S21E) and the Li dendrite penetration (fig. S21F). The unstable Li kinetics on nonalloying substrates can be attributed to the uneven interfacial contact and poor interfacial atom diffusion. The existence of chemical diffusion helps to remain a stable operation and suppresses the occurrence of dendrite penetration.

In particular, we compare the DRT of the R_{ct} with different critical Li content alloys (Al, In, and Sn), Li-Li and Li-Cu, which are all measured in all-solid-state batteries (fig. S22). As displayed in Fig. 6D, their DRT peaks exhibit similar relaxation time and intensity ratio, which can be treated as evidence for the Li metal precipitation in different alloys. The evaluation in other Li alloys demonstrates that the failure of multiple Li alloys is due to the Li precipitation by the

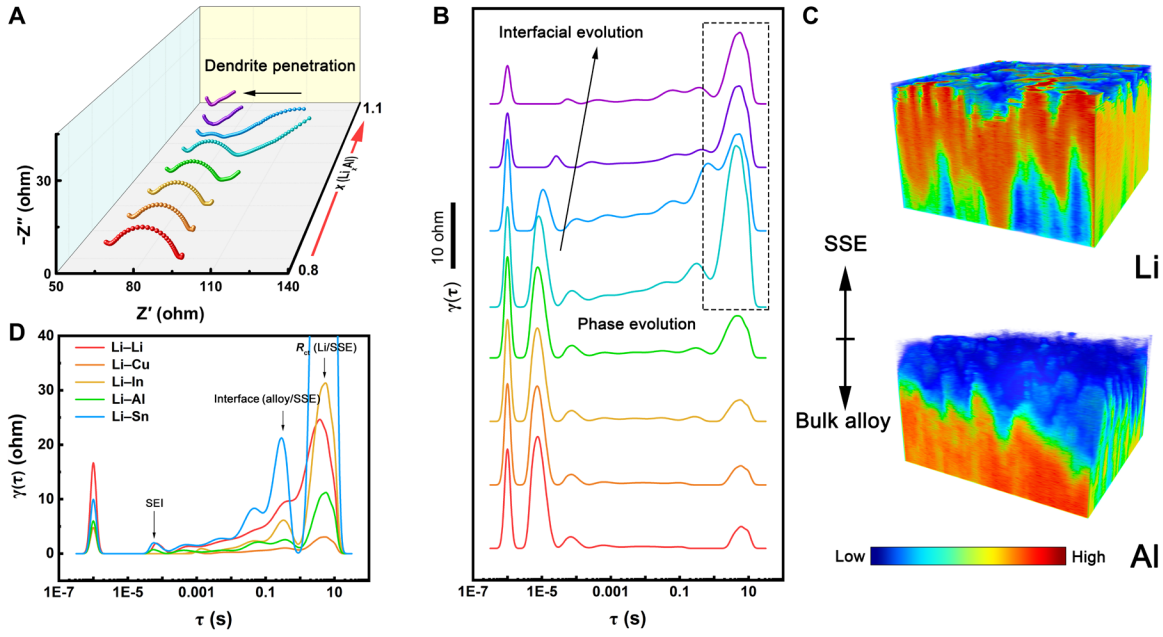

Fig. 6. Kinetic characteristics during lithiation in Li-Al alloy electrode in all-solid-state batteries. (**A**) GEIS evolution at the degradation stage of Li-Al alloy. (**B**) DRT transition of GEIS in (A). (**C**) Elemental distribution of Li and Al in a failed Li-Al alloy. The TOF-SIMS area is 50 μm by 50 μm. (**D**) Final stages of DRT plots for different Li alloys and Li metal anodes.

critical Li contents induced Li kinetic transition from alloying to deposition.

In summary, the Li kinetic feature of alloy anodes is quantitatively investigated in all-solid-state batteries with increasing Li contents, where a critical point is the carrier transition from Li atoms to vacancies. The high Li contents induced interfacial Li kinetic transition from Li alloying to deposition lead to the anodic failure in a typical Li alloy (e.g., Li-In, Li-Al, etc.) for all-solid-state batteries. By introducing advanced TOF-SIMS and in situ GEIS cooperating with DRT analysis, the interfacial charge transfer and Li^0 diffusion are ensured as the key Li kinetic steps for stabilizing the Li alloy interface during Li plating processes. The critical Li contents for Li alloy (e.g., $x = 1.25$ for Li_xIn and $x = 1$ for Li_xAl) are the triggers for Li kinetic transitions. The rate-determining steps for Li kinetic transition are judged by comparing the charge transfer induced voltage (0 V versus Li^+/Li) and the intrinsic Li^0 diffusion coefficient (10^{-11} cm^2 s^{-1}) of Li metal.

The Li alloys exhibit three charging stages with different rate-determining steps.

1) Stable alloying processes. Low charge transfer impedance induces rational alloying potential (> 0 V versus Li^+/Li) and rapid Li^0 diffusion (10^{-10} cm^2 s^{-1}) at low Li contents (e.g., $x < 1$ for Li_xIn), where Li atoms work as the carriers.

2) Charge transfer dominated process before critical Li contents (e.g., $1 < x < 1.25$ for Li_xIn). Charge transfer is the rate-determining step and there is a competition between two carriers leading to enlarged overpotential (>300 mV) and the transition from alloying to metal precipitation.

3) Li^0 diffusion dominated processes. Li atom transport is the rate-determining step when exceeding the critical Li contents (e.g., $x > 1.25$ for Li_xIn). The potential reaches 0 V versus Li/Li^+ with reduced Li^0 diffusion coefficient (<10^{-12} cm^2 s^{-1}), resulting in metal accumulation and interface failure. At this stage, Li^0 diffusion is restrained and Li vacancies work as the carriers.

The charge transfer triggers the kinetic transition from alloying to precipitation, and the Li^0 diffusion consolidates the Li precipitation. The Li kinetic characters also exhibit similarities in other Li alloys. It is concluded that low charge transfer barriers that induced anodic potential (≥ 0 V versus Li^+/Li) with rapid Li^0 diffusion (>10^{-11} cm^2 s^{-1}) for high Li-content Li alloy are essential to stabilize the Li alloy/SSE interfaces. The Li kinetic transition demonstrates the alternation of the domination carriers from Li atoms to Li vacancies in the bulk, constituting the internal cause of the specific kinetic features including the rate-determining step and interfacial stabilities. The knowledge of rate-determining steps and carriers in lithium alloy anodes provides the crucial insight needed for applications of next-generation solid-state lithium batteries.

MATERIALS AND METHODS

Experimental section

Battery assembly

The solid-state electrolyte $Li_7P_3S_{11}$ is purchased from Zhejiang Ningbo Linengxin New Materials Corp. Ltd. The $Li_7P_3S_{11}$ is cold-pressed at 360 MPa. During the operation of these all-solid-state batteries, the applied pressure provided by the battery mold is around 1 MPa. The counter/reference electrode (CE/RE) is 100-μm In foil with 100-μm Li foil. The LiIn phase is prepared by pressing the Li foil of ~3 mg and In foil of 57 mg together as electrodes in batteries. Li_2In phase is prepared by pressing Li foil of ~3 mg and In foil of 28 mg together as electrodes. Working electrode can be 20-μm In foil, as well as Al foil, Sn foil, Ti foil, and Cu foil. The battery is assembled as mold cells. Here, a two-electrode system is used for EIS analysis with a thick (100 μm) and stable LiIn alloy as lithium

source, CE, and RE. The working electrode is a thin In foil (20 μm). Using an "ideal" CE/RE in two electrode systems is also reported by Krauskopf *et al.* (*7*). First, the high stability of LiIn during lithium stripping is demonstrated by the symmetric cells, and the influence of CE/RE is clarified by impedance DRT analysis (fig. S8). The thick LiIn electrodes not only deliver a stable voltage plateau but also exhibit a low and stable impedance in continuous cycling, which is in consistence with the use of LiIn as RE in SSLMBs.

Characterization

The TOF-SIMS analysis is accomplished by TESCAN S9000 scanning electronic microscopy equipped with FIB and TOF-SIMS accessories. The measurement beams are ranged from 10 pA to 10 nA. The FIB is used to cut a cross section for TOF-SIMS imaging. The current for FIB is range from 50 to 500 nA. The FIB gun exhibits 55° angle with a TOF-SIMS detector. The in situ EIS is accomplished by Solartron Energy Lab XM. The EIS measurement is conducted in an amplitude of 10 mV with the frequency from 1 MHz to 0.1 Hz. The GEIS measurements are repetitively conducted after an equal interval in a discharge period of 0.1 mAh cm^{-2}. The DRT is conducted to distribute the specialized relaxation time in EIS spectra. The DRT analyses are conducted by the MATLAB GUI tool box developed by Ciucci's research team (*16*).

Identification of DRT peaks

The identification of DRT peaks in plots is the most essential step for DRT analyses. The distribution can be separated in three steps. First, the electrochemical ranges can be estimated by the experienced identification on relaxation time range. For instance, the high frequency of τ at 10^{-7} to 10^{-6} s can be attributed to the grain boundary response in a solid-state electrolyte. The lithium transport in SEI or different interfaces can be attributed to the response in 10^{-5} to 10^{-3} s. The R_{ct} is located at 10^{-2} to 10 s. This is summarized by Schmidt *et al.* (*14*). Second, the analyses on electrochemical system with single electrochemical process can identify its specialized relaxation time (DRT peak). DRT in a pure system can help to distinguish the specific relaxation time. The impedance spectra of pure $Li_7P_3S_{11}$ electrolytes, as well as symmetric cells of LiIn and Li-Li, are all interpreted by DRT tools to clearly distinguish the specialized relaxation time of electrolytes and electrodes with their specific interfaces. Figure S7 exhibited the DRT plots of $Li_7P_3S_{11}$. Figure S8 exhibited the impedance and the DRT plots of LiIn. In addition, an accurate identification on each electrochemical process is conducted by comparing the DRT peaks of continuous impedance in discharged and charged Li-In electrodes. Figure S9 displayed the discharge and charge profiles with impedance evolution. Then, the impedance in discharge and charge processes is interpreted by DRT. An obvious irreversible process is detected at τ of 10^{-3} s at the discharge process, and the specialized relaxation time remains stable at the charge process. It can be clearly ensured that the continuous evolution of DRT peak from 10^{-4} to 10^{-3} s is related to the formation process of SEI at initial lithium plating (lithiation) in Li-In. Then, the τ of 10^{-3} s remains stable at the charge process (delithiation), which is related to the stabilized SEI. The τ of 10^{-2} to 10^{-1} s exhibits completely reversible (fig. S10, C and D). Hence, this process can be affirmed as reversible evolution of R_{ct}.

Calculation of diffusion coefficient

The diffusion evolution is tracked based on the GITT. The relaxations in Li alloy system are mainly derived from the Li atom diffusion, which are demonstrated by Janek *et al.* (*10*). The diffusion coefficient based on Fick's law is evaluated by following simplified equation (Eqs. 5 and 6) (*19*, *37*, *38*)

$$D_{GITT} = \frac{4}{\pi\tau}\left(\frac{n_m V_m}{S}\right)^2\left(\frac{\Delta E_s}{\Delta E_t}\right)^2 \quad (5)$$

$$\tau \ll \frac{L^2}{D_{GITT}} \quad (6)$$

where τ represents the relaxation time, n_m represents the mole value and V_m is the mole volume, S is the contact area of electrode/electrolyte, ΔE_s is the voltage response stimulated by the pulse current, and ΔE_t is the voltage change by the galvanostatic discharge.

Phase field simulation

The phase field simulation is performed by COMSOL Multiphysics 5.5. The system is with a square size of 20 μm by 20 μm, in which the initial state is a two-phase system of the solid-state electrolyte above and pure In metal below. The detailed parameter setting and corresponding modeling for phase field simulation are provided in the Supplementary Materials.

DFT calculation

DFT calculations were performed to calculate defect formation energies of Li atoms in Li-rich Li-In alloys using the Vienna Ab initio Simulation Package (*39*). The projector augmented wave method was used to describe the ion-electron interactions (*40*). For the exchange-correlation energy, Perdew-Burke-Ernzerhof version of generalized gradient approximation was used (*41*). An energy cutoff of 500 eV was used for the plane wave expansion of the valence electron wave functions. A dense Γ-centered Monkhorst-Pack *k*-point mesh with a sampling density of 0.03 $Å^{-1}$, 10^{-6} eV/cell in energy, and 10^{-2} eV/Å in force for the convergence criterion was adopted during structural optimization. The initial crystalline structures of Li-rich Li-In alloys Li_5In_4 and Li_3In_2 were extracted from the Materials Project (*42*). After a careful structural optimization, the defect formation energies E_f of Li atoms were calculated on the basis of Eq. 7

$$E_f = E_{defect} - E_{perfect} - n\mu_{Li} \quad (7)$$

where E_{defect} and $E_{perfect}$ are the total energies of a lattice with a defect and a defect-free lattice, respectively. The integer n denotes the number of Li atoms that were added to ($n > 0$) or removed from ($n < 0$) the lattice to form the interstitial or vacancy, respectively. m_{Li} is the chemical potential of Li atom, which was set to the energy per atom in bulk Li lattice.

SUPPLEMENTARY MATERIALS

Supplementary material for this article is available at https://science.org/doi/10.1126/sciadv.abi5520

REFERENCES AND NOTES

1. X. B. Cheng, R. Zhang, C. Z. Zhao, Q. Zhang, Toward safe lithium metal anode in rechargeable batteries: A review. *Chem. Rev.* **117**, 10403–10473 (2017).
2. J. Zheng, Q. Zhao, T. Tang, J. Yin, C. D. Quilty, G. D. Renderos, X. Liu, Y. Deng, L. Wang, D. C. Bock, C. Jaye, D. Zhang, E. S. Takeuchi, K. J. Takeuchi, A. C. Marschilok, L. A. Archer, Reversible epitaxial electrodeposition of metals in battery anodes. *Science* **366**, 645–648 (2019).
3. T. Krauskopf, F. H. Richter, W. G. Zeier, J. Janek, Physicochemical concepts of the lithium metal anode in solid-state batteries. *Chem. Rev.* **120**, 7745–7794 (2020).
4. Y. Lu, X. Huang, Z. Song, K. Rui, Q. Wang, S. Gu, J. Yang, T. Xiu, M. E. Badding, Z. Wen, Highly stable garnet solid electrolyte based Li-S battery with modified anodic and cathodic interfaces. *Energy Storage Mater.* **15**, 282–290 (2018).
5. X.-Q. Zhang, X. Chen, L.-P. Hou, B.-Q. Li, X.-B. Cheng, J.-Q. Huang, Q. Zhang, Regulating anions in the solvation sheath of lithium ions for stable lithium metal batteries. *ACS Energy Lett.* **4**, 411–416 (2019).

6. N. J. J. de Klerk, M. Wagemaker, Space-charge layers in all-solid-state batteries; Important or negligible? *ACS Appl. Energy Mater.* **1**, 5609–5618 (2018).
7. T. Krauskopf, H. Hartmann, W. G. Zeier, J. Janek, Toward a fundamental understanding of the lithium metal anode in solid-state batteries—An electrochemo-mechanical study on the garnet-type solid electrolyte $Li_{6.25}Al_{0.25}La_3Zr_2O_{12}$. *ACS Appl. Mater. Interfaces* **11**, 14463–14477 (2019).
8. Y. Lu, C. Z. Zhao, H. Yuan, X. B. Cheng, J. Q. Huang, Q. Zhang, Critical current density in solid-state lithium metal batteries: Mechanism, influences, and strategies. *Adv. Funct. Mater.* **31**, 2009925 (2021).
9. T. Krauskopf, B. Mogwitz, H. Hartmann, D. K. Singh, W. G. Zeier, J. Janek, The fast charge transfer kinetics of the lithium metal anode on the garnet-type solid electrolyte $Li_{6.25}Al_{0.25}La_3Zr_2O_{12}$. *Adv. Energy. Mater.* **10**, 2000945 (2020).
10. T. Krauskopf, B. Mogwitz, C. Rosenbach, W. G. Zeier, J. Janek, Diffusion limitation of lithium metal and Li–Mg alloy anodes on LLZO type solid electrolytes as a function of temperature and pressure. *Adv. Energy Mater.* **9**, 1902568 (2019).
11. Y. Lu, X. Huang, Y. Ruan, Q. Wang, R. Kun, J. Yang, Z. Wen, An in situ element permeation constructed high endurance Li–LLZO interface at high current densities. *J. Mater. Chem. A* **6**, 18853–18858 (2018).
12. C. Yang, H. Xie, W. Ping, K. Fu, B. Liu, J. Rao, J. Dai, C. Wang, G. Pastel, L. Hu, An electron/ion dual-conductive alloy framework for high-rate and high-capacity solid-state lithium-metal batteries. *Adv. Mater.* **31**, 1804815 (2019).
13. J. Wan, Y. X. Song, W. P. Chen, H. J. Guo, Y. Shi, Y. J. Guo, J. L. Shi, Y. G. Guo, F. F. Jia, F. Y. Wang, R. Wen, L. J. Wan, Micromechanism in all-solid-state alloy-metal batteries: Regulating homogeneous lithium precipitation and flexible solid electrolyte interphase evolution. *J. Am. Chem. Soc.* **143**, 839–848 (2021).
14. J. P. Schmidt, T. Chrobak, M. Ender, J. Illig, D. Klotz, E. Ivers-Tiffée, Studies on $LiFePO_4$ as cathode material using impedance spectroscopy. *J. Power Sources* **196**, 5342–5348 (2011).
15. F. Ciucci, Modeling electrochemical impedance spectroscopy. *Curr. Opin. Electrochem.* **13**, 132–139 (2019).
16. T. H. Wan, M. Saccoccio, C. Chen, F. Ciucci, Influence of the discretization methods on the distribution of relaxation times deconvolution: Implementing radial basis functions with DRTtools. *Electrochim. Acta* **184**, 483–499 (2015).
17. Y. Zhang, Y. Chen, M. Yan, F. Chen, Reconstruction of relaxation time distribution from linear electrochemical impedance spectroscopy. *J. Power Sources* **283**, 464–477 (2015).
18. F. Dion, A. Lasia, The use of regularization methods in the deconvolution of underlying distributions in electrochemical processes. *J. Electroanal. Chem.* **475**, 28–37 (1999).
19. A. Nickol, T. Schied, C. Heubner, M. Schneider, A. Michaelis, M. Bobeth, G. Cuniberti, GITT analysis of lithium insertion cathodes for determining the lithium diffusion coefficient at low temperature: Challenges and pitfalls. *J. Electrochem. Soc.* **167**, 090546 (2020).
20. P. Adeli, J. D. Bazak, K. H. Park, I. Kochetkov, A. Huq, G. R. Goward, L. F. Nazar, Boosting solid-state diffusivity and conductivity in lithium superionic argyrodites by halide substitution. *Angew. Chem. Int. Ed.* **58**, 8681–8686 (2019).
21. M. D. Berliner, B. C. McGill, M. Majeed, D. T. Hallinan, Electrochemical kinetics of lithium plating and stripping in solid polymer electrolytes: Pulsed voltammetry. *J. Electrochem. Soc.* **166**, A297–A304 (2019).
22. D. M. Fischer, P. Duwe, S. Indris, P. Heitjans, Tracer diffusion measurements in solid lithium: A test case for the comparison between NMR in static and pulsed magnetic field gradients after upgrading a standard solid state NMR spectrometer. *Solid State Nucl. Magn. Reson.* **26**, 74–83 (2004).
23. V. Schott, M. Fähnle, P. A. Madden, Theory of self-diffusion in alkali metals: I. Results for monovacancies in Li, Na, and K. *J. Phys. Condens. Mat.* **12**, 1171–1194 (2000).
24. F. Lantelme, Y. Iwadate, Y. Shi, M. Chemla, Electrochemical investigation of interdiffusion in Al + Li alloys. *J. Electroanal. Chem.* **187**, 229–246 (1985).
25. Q. Wang, G. Zhang, Y. Li, Z. Hong, D. Wang, S. Shi, Application of phase-field method in rechargeable batteries. *npj Comput. Mater.* **6**, 176 (2020).
26. D. R. Ely, A. Jana, R. E. García, Phase field kinetics of lithium electrodeposits. *J. Power Sources* **272**, 581–594 (2014).
27. A. L. Santhosha, L. Medenbach, J. R. Buchheim, P. Adelhelm, The indium-lithium electrode in solid-state lithium-ion batteries: Phase formation, redox potentials, and interface stability. *Batter. Supercaps* **2**, 524–529 (2019).
28. K. Yan, Z. Lu, H. W. Lee, F. Xiong, P. C. Hsu, Y. Li, J. Zhao, S. Chu, Y. Cui, Selective deposition and stable encapsulation of lithium through heterogeneous seeded growth. *Nat. Energy* **1**, 16010 (2016).
29. A. Pei, G. Zheng, F. Shi, Y. Li, Y. Cui, Nanoscale nucleation and growth of electrodeposited lithium metal. *Nano Lett.* **17**, 1132–1139 (2017).
30. A. Van der Ven, J. Bhattacharya, A. A. Belak, Understanding Li diffusion in Li-intercalation compounds. *Acc. Chem. Res.* **46**, 1216–1225 (2013).
31. Y. Zhang, K. S. R. Chandran, M. Jagannathan, H. Z. Bilheux, J. C. Bilheux, The nature of electrochemical delithiation of Li-Mg alloy electrodes: Neutron computed tomography and analytical modeling of Li diffusion and delithiation phenomenon. *J. Electrochem. Soc.* **164**, A28–A38 (2017).
32. A. Urban, D.-H. Seo, G. Ceder, Computational understanding of Li-ion batteries. *npj Comput. Mater.* **2**, 16002 (2016).
33. M. Yang, Y. Liu, A. M. Nolan, Y. Mo, Interfacial atomistic mechanisms of lithium metal stripping and plating in solid-state batteries. *Adv. Mater.* **33**, 2008081 (2021).
34. W. Frank, U. Breier, C. Elsasser, M. Fahnle, First-principles calculations of absolute concentrations and self-diffusion constants of vacancies in lithium. *Phys. Rev. Lett.* **77**, 518–521 (1996).
35. M. Z. Ghavidel, M. R. Kupsta, J. le, E. Feygin, A. Espitia, M. D. Fleischauer, Electrochemical formation of four Al-Li phases (β-AlLi, Al_2Li_3, $AlLi_{2-x}$, Al_4Li_9) at intermediate temperatures. *J. Electrochem. Soc.* **166**, A4034–A4040 (2019).
36. W. Gasior, Z. Moser, Chemical diffusion coefficients in solid Al-Li alloys at low Li concentrations. *Scand. J. Metall.* **31**, 353–358 (2002).
37. Y. Zhu, C. Wang, Galvanostatic intermittent titration technique for phase-transformation electrodes. *J. Phys. Chem. C* **114**, 2830–2841 (2010).
38. Z. Shen, L. Cao, C. D. Rahn, C.-Y. Wang, Least squares galvanostatic intermittent titration technique (LS-GITT) for accurate solid phase diffusivity measurement. *J. Electrochem. Soc.* **160**, A1842–A1846 (2013).
39. G. Kresse, J. Furthmüller, Efficiency of ab-initio total energy calculations for metals and semiconductors using a plane-wave basis set. *Comput. Mater. Sci.* **6**, 15–50 (1996).
40. P. E. Blöchl, Projector augmented-wave method. *Phys. Rev. B* **50**, 17953–17979 (1994).
41. J. P. Perdew, K. Burke, M. Ernzerhof, Generalized gradient approximation made simple. *Phys. Rev. Lett.* **77**, 3865–3868 (1996).
42. A. Jain, S. P. Ong, G. Hautier, W. Chen, W. D. Richards, S. Dacek, S. Cholia, D. Gunter, D. Skinner, G. Ceder, K. A. Persson, Commentary: The Materials Project: A materials genome approach to accelerating materials innovation. *APL Mater.* **1**, 011002 (2013).

Acknowledgments: We thank X.-M. Xu and Y.-T. Chen for the suggestions about characterizations. **Funding:** This work was supported by National Natural Science Foundation of China (21825501 and U1801257), Beijing Municipal Natural Science Foundation (Z20J00043), National Key Research and Development Program (2016YFA0202500), China Postdoctoral Science Foundation (2019 M660659 and BX20190168), and The Shuimu Tsinghua Scholar Program Tsinghua University Initiative Scientific Research Program. **Author contributions:** Conceptualization: Q.Z. and Y.L. Methodology: Y.L. and L.-P.H. Investigation: Y.L. Phase field simulation: R.Z. Mechanism interpretation: X.C. and Z.-H.F. DFT calculation: Z.-H.F. Supervision: Q.Z. Writing—original draft: Y.L. and C.-Z.Z. Writing—review and editing: Y.L., C.-Z.Z., H.Y., Q.Z., and J.-Q.H. **Competing interests:** The authors declare that they have no competing interests. **Data and materials availability:** All data needed to evaluate the conclusions in the paper are present in the paper and/or the Supplementary Materials.

Submitted 16 March 2021
Accepted 23 July 2021
Published 15 September 2021
10.1126/sciadv.abi5520

Citation: Y. Lu, C.-Z. Zhao, R. Zhang, H. Yuan, L.-P. Hou, Z.-H. Fu, X. Chen, J.-Q. Huang, Q. Zhang, The carrier transition from Li atoms to Li vacancies in solid-state lithium alloy anodes. *Sci. Adv.* **7**, eabi5520 (2021).

ScienceAdvances

The carrier transition from Li atoms to Li vacancies in solid-state lithium alloy anodes

Yang LuChen-Zi ZhaoRui ZhangHong YuanLi-Peng HouZhong-Heng FuXiang ChenJia-Qi HuangQiang Zhang

Sci. Adv., 7 (38), eabi5520. • DOI: 10.1126/sciadv.abi5520

Science Advances (ISSN) is published by the American Association for the Advancement of Science. 1200 New York Avenue NW, Washington, DC 20005. The title *Science Advances* is a registered trademark of AAAS.